Research Article Vol. 11, No. 8 / 1 August 2020 / *Biomedical Optics Express* 4379

Biomedical Optics EXPRESS

Second harmonic generation characterization of collagen in whole bone

EMILY G. PENDLETON,[1] KAYVAN F. TEHRANI,[1] RUTH P. BARROW,[1] AND LUKE J. MORTENSEN[1,2,*]

[1] *Regenerative Bioscience Center, Rhodes Center for ADS, University of Georgia, Athens, GA 30602, USA*
[2] *School of Chemical, Materials and Biomedical Engineering, University of Georgia, Athens, GA 30602, USA*
[*] *Luke.Mortensen@uga.edu*

Abstract: Bone is a unique biological composite material made up of a highly structured collagen mesh matrix and mineral deposits. Although mineral provides stiffness, collagen's secondary organization provides a critical role in bone elasticity. Here, we performed polarimetric analysis of bone collagen fibers using second harmonic generation (SHG) imaging to evaluate lamella sheets and collagen fiber integrity in intact cranial bone. Our polarimetric data was fitted to a model accounting for diattenuation, polarization cross-talk, and birefringence. We compared our data to the fitted model and found no significant difference between our polarimetric observation and the representation of these scattering properties up to 70 μm deep. We also observed a loss of resolution as we imaged up to 70 μm deep into bone but a conservation of polarimetric response. Polarimetric SHG allows for the discrimination of collagen lamellar sheet structures in intact bone. Our work could allow for label-free identification of disease states and monitor the efficacy of therapies for bone disorders.

1. Introduction

Mammalian bone has a complex composite material structure consisting of an aqueous collagen fiber mesh integrated with a hard hydroxyapatite mineral phase [1]. This combination of components is critical to the unique mechanical properties of bone, with toughness provided by the elastic collagen fibers and stiffness from the mineral content. The mechanical properties of a composite material are dependent on the arrangement of the reinforcing phase, and so the organization of bone collagen plays an essential role in the overall bone mechanics and fracture risk [2]. Emerging research supports that collagen mesh microarchitecture is disrupted in multiple diseases with associated bone fragility, such as osteoporosis, type II diabetes, and osteogenesis imperfecta [3–5]. Therefore, strategies such as second harmonic generation (SHG) that could investigate the organization of the critically important collagen mesh matrix microarchitecture are needed.

SHG is a label-free non-linear coherent imaging strategy useful for non-centrosymmetric structures, such as type I collagen. Exposure of the collagen fibers to high energy laser pulses generates an emission signal at twice the excitation frequency by collagen molecules whose α-helix pitch angles are at roughly 50° from the direction of the polarization excitatory pulses [6,7]. These triple helix collagen molecules are produced within the cell and transported to the extracellular space where they form collagen fibrils. The long axis of the molecules is parallel to the long axis of the collagen fibrils [8]. The relative intensity of SHG signal is dependent on the orientation of collagen relative to the polarized excitation light (Fig. 1) [9]. Thus, the resulting SHG image is of an overall higher intensity when the excitation light is oriented to highlight the molecular and fiber direction. The relative intensity of the collagen fiber excitation from fundamental properties can be described by anisotropy which explains the orientation of proteins in tissues [10]. Bone collagen fibrils assemble themselves in the extracellular space into fiber

#391866 https://doi.org/10.1364/BOE.391866
Journal © 2020 Received 2 Mar 2020; revised 10 Jun 2020; accepted 16 Jun 2020; published 17 Jul 2020

bundles, which are arranged in plywood-like layers called lamella [8,11]. The fibers within the lamella lay parallel to each other and at angles to adjacent layers of lamella [8], which provides a framework for the deposition of bone mineral hydroxyapatite crystals that strengthen the bone [12]. Therefore, SHG could be useful in describing structural collagen information and could provide insight into secondary bundling of collagen fibers [13].

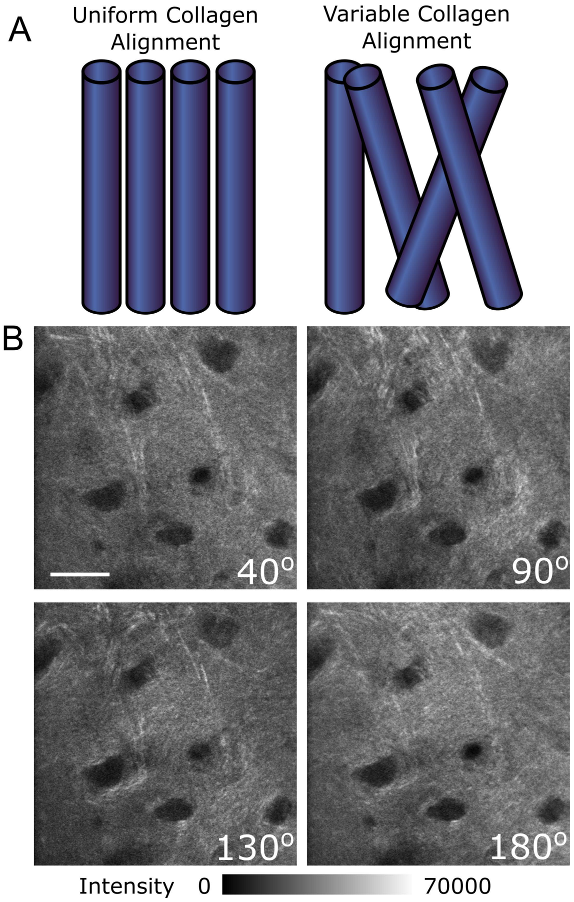

Fig. 1. The strength of the second harmonic signal is dependent on the orientation of collagen relative to the polarized light. (A) SHG signal will change with the angle of polarized light when collagen fibers are aligned but not when there is variable orientation. (B) When the light is parallel to the dominant orientation of collagen fibers, here at 90°, these fibers will generate strong second harmonic signal. The SHG signal is dimmest when it is perpendicular to the dominant orientation of collagen fibers (180°). At intermediate angles, 40° and 130°, collagen fibers of different orientations create second harmonic signal. Scale bar: 20 μm.

SHG imaging has been used in bone to evaluate features that change during growth and development, including an increase in osteons and fiber structure organization [14]. SHG has also been used in conjunction with third harmonic generation (THG) in order to evaluate the lacuno-canalicular network [15]. SHG is compatible with two-photon fluorescence imaging, and together, they have been used to relate microcracking to lamellar sheet structures of osteonal bone [16]. However, in each of these instances the bone underwent substantial processing that would preclude intravital use or analysis was confined to the surface of the bone [14–16]. In other collagen-rich tissues such as skin, muscle, tendon, and bone, SHG with linearly polarized or circularly polarized excitation light has been used for label-free analysis of collagen fiber organization [17–19], typically after tissue sectioning [20]. The sensitivity of SHG imaging to collagen organization is promising for diagnostic and prognostic imaging of disease in these tissues [13,21–23]; ranging from cancer [24], to metabolic bone disorders like osteogenesis imperfecta [25], to osteoarthritis [26], to corneal disease [27]. Efforts to image the collagen mesh structure in full thickness tissues like tendon [28] or artery [29] require additional knowledge of the samples and correction to extract accurate orientation measures due to scattering and distortions of the excitation beam and the epi-detected second harmonic signal. Due to the challenges posed by the short mean-free-path of bone, limited attention has been paid to the potential of polarization resolved SHG to evaluate collagen fiber organization in intact three dimensional mineralized bone tissue.

In this work, we investigate the potential of polarimetric SHG to provide insight into intact cranial bone collagen organization with linearly polarized excitation light. We evaluate the depth limitations of SHG in the cranial bone first by probing intensity contrast and frequency content through 70 μm of cranial bone, and then evaluating the fidelity of polarization contrast through the bone using polarization resolved detection to estimate tissue distortions due to diattenuation, birefringence, and polarization cross-talk up to a depth of 70 μm. Despite a significant reduction in resolution and image information content, we characterize structural information about bone collagen beyond the mean-free-path of bone up to a depth of 70 μm. Close to the surface of the bone, we are able to resolve collagen organization across a field of view, to discriminate lamellar sheet angle and integrity, as well as to identify discrete groups of collagen fiber bundles. The use of polarimetric SHG imaging enables the discrimination of fiber bundle orientation 70 μm deep in the bone beyond our observed mean-free-path of 43.47 μm [30]. Our results show that SHG polarimetry can be used to effectively discriminate collagen lamellar sheet structures in intact cranial bone tissue. These findings could enable future work on label-free identification of disease states of the bone and monitor effectiveness of therapies for bone disorders like hypophosphatasia, osteogenesis imperfecta, X-linked hypophosphatemia, or osteoporosis.

2. Theory

2.1. Polarimetric SHG of bone

The SHG signal ($I^{2\omega}$) is linked to the electric field (E^2) by the second order nonlinear susceptibility tensor χ^2 [31]:

$$I^{2\omega} = X^2_{ijk} E^2 \tag{1}$$

Where *i, j, k* are the spatial directions *x, y, z*. The second order nonlinear susceptibility tensor is defined by:

$$X^2_{ijk} E^2 = N_s {<}\beta{>} \tag{2}$$

Here, N_s is the density of molecules and $<\beta>$ is the average molecular hyperpolarizability [10]. We assume that the collagen fibers along the x-axis have cylindrical symmetry and Kleinmann symmetry such that the tensor χ^2 has two components: $\chi^{(2)}{}_{xxx}$ and $\chi^{(2)}{}_{xyy}=\chi^{(2)}{}_{xzz}=\chi^{(2)}{}_{yxy}=\chi^{(2)}{}_{zxz}=\chi^{(2)}{}_{yyx}=\chi^{(2)}{}_{zzx}$ [10]. With this knowledge, the back-detected SHG intensity can be described as

$$I^{2\omega}_x \propto \rho\, cos^2(\alpha - \varphi) + sin^2(\alpha - \varphi) \tag{3}$$

$$I^{2\omega}_y \propto 2cos(\alpha - \varphi) sin(\alpha - \varphi) \tag{4}$$

where $\rho = {}^{\chi^{(2)}_{xxx}}/{}_{\chi^{(2)}_{xyy}}$ is the anisotropy parameter and φ is the angle of orientation of the collagen fibrils with respect to the x-axis when the incident electric field is at angle α [31].

2.2. Confounding effects of SHG: birefringence, diattenuation and polarization cross-talk

To explore the potential distortions of the detected SHG signal by cranial bone tissue and to evaluate if additional correction is needed, we used an adult mouse skull with the x and y components of the epi-detected SHG signal separated using a polarizing beam splitter where the x component was parallel to the excitation light and the y component was perpendicular [32]. Linearly polarized excitation light was rotated over 180° at 10° increments every 5 μm of depth from the surface through 70 μm of intact bone. The intensity of the x component of the epi-detected SHG signal was collected and filtered using a Fourier triangle mask to limit analysis to objects of similar orientation, with an apex angle of 44°. We evaluated the intensity created across every 10° of light at a given depth by fitting with the generalized functions as described previously by Gusachenko, et al. [32]

$$I_x^{2\omega} = Acos(4\alpha) + Bcos(2\alpha) + C \tag{5}$$

$$I_y^{2\omega} = \frac{K}{2}(-cos(4\alpha) + 1) \tag{6}$$

Where

$$A = \frac{K}{2}\left(\frac{\rho - 1}{2}\right)^2 \tag{7}$$

$$B = 2K\left(\frac{\rho - 1}{2}\right)\left(\frac{\rho + 1}{2}\right) \tag{8}$$

$$C = \frac{K}{2}\left(\frac{\rho - 1}{2}\right)^2 + \left(\frac{\rho + 1}{2}\right)^2 \tag{9}$$

Solving for each variable allowed us to describe the ordering of collagen molecules with ρ, the ratio of the two main tensorial components as

$$\rho^2 = \frac{X_{xxx}^{(2)}}{X_{xyy}^{(2)}} = \frac{A + B + C}{A - B + C} \tag{10}$$

This simplified set of equations does not take the heterogeneous tissue optical properties of the bone into account, so we then investigated the contributions of diattenuation (Δl_{a}), birefringence (Δn), and polarization cross-talk (η) to the x component of the detected SHG signal. Diattentuation, or a difference in the mean-free-path of excitation light at 0° and 90° from the x component, can impact the detection of collagen depending on its orientation. To determine diattenuation of SHG signal in bone, we determined the mean-free-path of excitation light at 0° and 90° from the x component. To describe both birefringence and excitation propagation, we used $\Delta\varphi = {}^{4\pi(\Delta n)z)}/_{\lambda}$, where λ is the excitation wavelength and z is depth. Polarization scrambling by the tissue, such that light that was initially polarized in the y direction becomes scattered and polarized in the x direction, may also alter the detected angle of collagen fibers in the tissue [32]. To consider these effects of birefringence and polarization cross-talk, we used the following equation:

$$I_x^{2\omega}(z) = Ke^{-\frac{2z}{l_a^0}}\left(|\rho e^{-\frac{z}{\Delta l_a}} cos^2\alpha e^{i\Delta\phi} + sin^2\alpha|^2 + \eta e^{-\frac{z}{\Delta l_a}}|sin2\alpha|^2\right) \tag{11}$$

Since polarization cross-talk and birefringence cannot be separated at a given depth, we used the variable, Δ, as proposed in Gusachenko, et al. [32] to determine the combined effect of birefringence and polarization cross-talk as a function of depth:

$$\Delta = \frac{C - 3A - \sqrt{(A + C)^2 - B^2}}{2(A - B + C)} \tag{12}$$

2.3. Angular distribution of collagen fibers

To allow quantitative approximation of the dominant collagen directionality in the excited volume, we continued to use a single linear polarization of excitation light that was rotated to generate polarimetric information with epi-collection of all generated second harmonic signal at each excitation angle by removing the polarizing beam splitter. We then fit a mathematical model of SHG intensity to our experimental values using Eqs. (3) and (4) when the collagen fibrils of the bone and electric field are in the focal plane [31]. Thus, the complete SHG signal can be described as:

$$I^{2\omega}(\alpha) = \beta[A cos(4\alpha - 4\varphi) + B cos(2\alpha - 2\varphi) + 1] \tag{13}$$

Where A and B are coefficients related to susceptibility components and β is the average number of detected photons [10]. Angular distribution of collagen fiber orientation, φ, was determined using incident polarized light, α, of 10-180° in increments of 10°.

3. Experimental methods

3.1. Animals

All animal experiments were approved by The University of Georgia Institutional Animal Care and Use Committee. The skulls of the specimens were embedded in silicone to prevent movement. Samples were stored in 70% ethanol at room temperature and hydrated with PBS throughout imaging.

3.2. Scanning electron microscopy

To provide a direct physical measurement of cranial bone lamellar sheet structure, we performed scanning electron microscopy (SEM). Fresh skulls were snap frozen and freeze fractured before dehydration in a vacuum. Samples were then carbon coated and mounted for SEM analysis using a Zeiss 1450EP.

3.3. Optical setup

Calvarial imaging experiments used a two-photon microscope described in our previous efforts (Fig. 2) [30]. The optical setup consists of a Calmar fiber laser producing 1550 nm 370 fs pulses of 3 μJ energy, with power at the source modulated using a half wave-plate and a polarizing beam splitter (PBS). The light was focused on a 1 mm bismuth triborate (BiBo) crystal to double the frequency to 775 nm, then recollimated and passed through a Pockels cell (Conoptics) for rapid intensity modulation during imaging. The beam was expanded using a telescope with a pinhole in the focus to create a more uniformly Gaussian x,y beam. The polarization angle was rotated using a half wave-plate in a motorized rotational mount (mrm) in the infinity space. The beam was scanned with a galvo and resonant galvo pair (Sutter) operating at 15 frames per second, and conjugated to the objective. Both the excitation and emission paths passed through a 60x Olympus objective with a 1.1 NA (LUMFLN60XW). SHG was collection by a PMT (Hamamatsu) with a 390/18 bandpass filter (Fig. 2(A)). For experiments in sections 3.6 and 4.1.2, a PBS was placed before the PMT (Fig. 2(B)). For most images we averaged 75 frames for every 10° of polarization; therefore, each polarimetric stack took approximately 90 seconds to acquire. At the start of each imaging session, we acquired polarimetric fluorescence images using a dilute solution of carboxyfluorescein succinimidyl ester (CFSE) to help correct for illumination and collection intensity differences that may result in the system as a function of polarization sensitivity.

SHG images (1024 x 1024 pixels) of collagen bone structure were produced with linearly polarized excitation, using a half wave-plate rotated to collect light at 10° intervals within the system to evaluate collagen fiber orientation. Representative Z-stacks of each mouse skull were generated through the thickness of the calvaria.

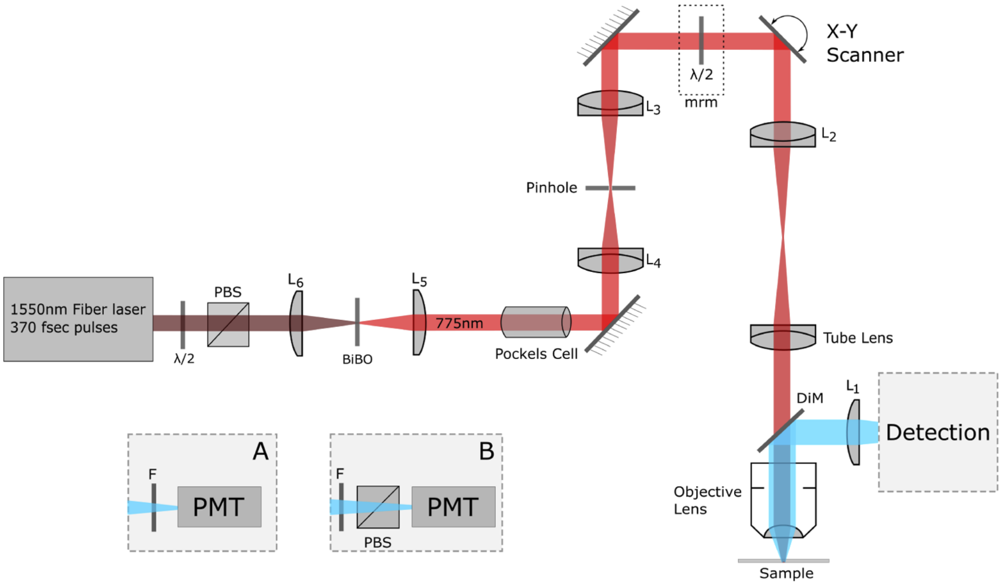

Fig. 2. Optical setup of the two-photon microscope. The red path is the excitation light and the blue path is the SHG emission. Mrm: motorized rotational mount, DiM: Dichroic mirror, BiBo: Bismuth triborate, PMT: Photon multiplier tube, L: Lens, F: Filter, PBS: Polarizing Beam Splitter. Detection path (A) was used unless otherwise noted. A PBS was added to the detection path (B) to evaluate polarization contrast through depth in sections 3.5 and 4.1.2.

3.4. Visualization of collagen fiber orientation

ImageJ 1.50e (Wayne Rasband, National Institute of Heath, USA) and MatLab (Matlab and Statistics Toolbox Release R2017a, The MathWorks Inc., Natick, MA, USA) were used to analyze stacks of angle-encoded images to visualize collagen lamellar orientation. To form the color images, we used images of our CFSE standard to compute A and B of Eq. (13). We then normalized each polarimetric stack to the CFSE standard reciprocal and fitted Eq. (13) to each pixel to determine the angle φ of collagen fiber orientation. The resulting 2-D image contained values of orientation rather than intensity. Every 10° was assigned a different color and multiplied by our gray-scale SHG average intensity image to pseudo-color.

3.5. Frequency domain resolution analysis

Multiple measures were performed to evaluate the impact of depth within full-thickness bone on resolution. We first evaluated the polarization and rotation of the light in the sample plane by imaging the surface of linear tendon and muscle fiber samples as has been suggested in prior work by Lien et al. [33], and found good agreement. We then investigated the frequency space of objects in the collagen fiber size range of bone as a function of imaging depth. The overall impact of cranial bone tissue on the frequency content of our SHG images as a function of depth provides a more comprehensive evaluation of the impact of the bone tissue on image quality. We collected three stacks of images from whole cranial bone of at least three wild type mice 8-12 weeks for each analysis. Images were acquired from regions dorsal to the cranial suture, from 10 μm to 70 μm below the periosteum. We avoided osteocyte lacunae by selecting 4 representative ROI's containing SHG signal within each image to use for further analysis.

The information content at each axial section within the cranial bone is first characterized by frequency bandwidth. The spatial domain $i(x,y)$ was converted to the 2-D Fourier domain power spectrum $I(\mu, \nu)$ at each depth. We performed a curve fitting analysis using an open source

Matlab code, “Fit 2-D gaussian function to data,” to rotate the angle ϕ a 2-D gaussian profile F about the center ϵ of the power spectrum to fit the long and short axis of the power spectrum. We then defined bandwidth as the reciprocal of the length of the long axis. The fitting is described with the following equations,

$$\mu^r = \mu\cos\phi - \nu\sin\phi \tag{14}$$

$$\nu^r = \mu\sin\phi + \nu\cos\phi \tag{15}$$

$$\epsilon_\mu^r = \epsilon_\mu\cos\phi - \epsilon_\nu\sin\phi \tag{16}$$

$$\epsilon_\nu^r = \epsilon_\mu\sin\phi + \epsilon_\nu\cos\phi \tag{17}$$

$$F = Aexp\left(-\left(\frac{\left(\mu^r - \epsilon_\mu^r\right)^2}{2{\sigma_\mu}^2} + \frac{\left(\nu^r - \epsilon_\nu^r\right)^2}{2{\sigma_\nu}^2}\right)\right) \tag{18}$$

$$\sigma = max\left([\sigma_\mu, \sigma_\nu]\right)^{-1} \cdot \frac{1}{nxdx} \tag{19}$$

To quantify the loss of resolution with depth we used a frequency content (FC) metric, based on our previous efforts [34]. The FC metric converts images from the spatial domain $i(x,y)$ to the Fourier domain $I(\mu, \nu)$, and filters the frequency contents to find the ratio of the contents of interest to all the frequency contents. It uses a band pass filter that consists of a high-pass filter with an inverse Gaussian profile $G(\mu, \nu)$, and a hard cut-off low-pass filter $M(\mu, \nu)$. The inverse Gaussian filter enables us to give unique weight to low and high frequency contents, to make a better characterization of both low and high frequency components. The filter is described using the following equations,

$$I(\mu, \nu) = \mathcal{F}\{i(x, y)\}, \tag{20}$$

$$FC = \sqrt{\frac{\sum_{\mu,\nu}\left(G(\mu, \nu)|I(\mu, \nu)|M(\mu, \nu)\right)^2}{\sum_{\mu,\nu}|I(\mu, \nu)|M(\mu, \nu)^2}}, \tag{21}$$

$$G(\mu, \nu) = 1 - exp\left(\frac{\mu^2 + \nu^2}{2\sigma^2}\right), \tag{22}$$

$$M(\mu, \nu) = \begin{cases} 1 & \sqrt{\mu^2 + \nu^2} < f_{co} \\ 0 & \text{otherwise} \end{cases}, \tag{23}$$

where f_{co} is the high cut-off frequency, the lower bound of the filter is defined by σ of the Gaussian filter, and $\mathcal{F}$ is the Fourier transform operator. For our analysis we determined $f_{co} = 0.93\ \mu\text{m}^{-1}$ based on our measurement of the diameter of collagen fibers seen at the surface of the bone, and the value of sigma was empirically set to $0.1\ \mu\text{m}^{-1}$ to get the highest contrast.

3.6. Polarization contrast through depth

To use SHG polarimetry to evaluate collagen fiber orientation, the optical setup was changed to collect all orientations of generated second harmonic signal (Fig. 2(B)). Linearly polarized excitation light was rotated with a half-wave plate and was collected every 5 μm from the surface to 70 μm deep. The transmitted channel was processed with a 3-D Gaussian blur (σ=1.5), normalized to the CFSE standard, and converted to the frequency domain. A triangle filter was used to include all objects within the frequency cutoffs that were directionally aligned with the collection channel. Filtering was necessary to reduce the influence of noise and potentially interfering SHG signal from collagen fibers oriented at different angles on our analysis, so we used the minimum size that provided adequate signal for our analysis (apex angle width of 44° in our case). The image was then converted back to the spatial domain, an Otsu threshold was applied, and the normalized intensity at every 10° was measured. The polarization mediated intensity variance is a calculated percentage of the intensity standard deviation across all angles of polarized light divided by the mean intensity:

$$o(x,y) = \frac{\sqrt{\frac{1}{N_p-1}\Sigma_P \left(i(x,y,p) - \mu_p(x,y)\right)^2}}{\mu_p(x,y)} \tag{24}$$

$$\mu_p(x,y) = \frac{1}{N_p}\Sigma\, i(x,y,p) \tag{25}$$

4. Results

4.1. Cranial SHG image quality as a function of depth

4.1.1. Spatial and frequency domain image quality measurements

We first investigated the object discrimination and effects of tissue aberrations and scattering on the focal quality and overall information content of our images in the first two mean-free-paths of cranial bone. To evaluate the quality of the focus, we imaged the SHG detected spot as a function of depth (Fig. 3(A)). We measured this width and normalized it with the width close to the surface. As we go deeper, the detected spot width increases which demonstrates that within one mean-free-path (~43 μm) [30] from the surface, the integration of back-scattered light contributes to the PSF. Thus the effective width produced is composed of forward-generated-back-scattered and backward-generated SHG signal, and the increased detected spot size with depth is induced by multiple scattering events and other wave-front distortions caused by the bone tissue. We also measured the normality of the Gaussian fit (R^2 values; Fig. 3(A), red dots), which interestingly shows a highly Gaussian shape of the detected spot within the first mean-free-path, and low correlation beyond that.

We calculated the power spectral bandwidth using the Fourier transform power spectrum for each ROI (Fig. 3(B)). We observed a decrease in the power spectral bandwidth as we imaged deeper into the bone. Compared to the surface (0.576 ± 0.156 μm^{-1}), the spatial frequency content of the images was significantly reduced at 10 μm deep (0.554 ± 0.151 μm^{-1}) and 30 μm of depth (0.407 ± 0.074 μm^{-1}) ($p < 0.05$ and $p < 0.01$, respectively). The bandwidth was further reduced at 60 μm (0.306 ± 0.047 μm^{-1}) and 70 μm depth (0.295 ± 0.0322 μm^{-1}), and was significantly different when compared with 20 μm (0.460 ± 0.086 μm^{-1}) ($p < 0.05$ and $p < 0.01$, respectively).

The average collagen fiber widths seen on the SHG images were then analyzed. At 0 μm, 5 μm, 10 μm, 15 μm, and 20 μm from the surface, five collagen fibers were randomly selected and a line was drawn perpendicular to its length. A Gaussian curve was fitted to the intensity profile of that line. The full width half max (FWHM) for each fiber was determined and the average FWHM for each depth was computed (Fig. 3(C)). We find fibers within the first 20 μm of the surface of the bone with FWHM measurements and Gaussian fits of 0.551 ± 0.153 μm, 0.531 ± 0.0809 μm, 0.572 ± 0.234 μm, 0.515 ± 0.161 μm, and 0.692 ± 0.302 μm at 0 μm, 5 μm, 10 μm, 15 μm, and 20 μm, respectively, which are comparable to published values for bone collagen fibers [8,15,35]. This average collagen fiber size was used to establish the high cut-off frequency for FC analysis.

There was significant difference in the collagen FC between the surface (0.103 ± 0.0167) and depths 30 – 70 μm (0.0734 ± 0.00649, 0.0639 ± 0.00566, 0.0644 ± 0.00840, 0.0515 ± 0.00651, 0.0511 ± 0.00693, respectively) (Fig. 3(D); $p < 0.05$). This suggests that images taken 10 μm (0.0857 ± 0.0110) and 20 μm (0.0788 ± 0.00335) deep contain significantly more frequency content in the range characteristic of collagen fibers than images acquired at 60 μm and 70 μm of depth ($p < 0.05$). All reported values are average ± standard deviation.

The reduction in frequency content and contrast as a function of depth is caused by tissue aberrations and scattering, and results in the simultaneous excitation of multiple fibers, which

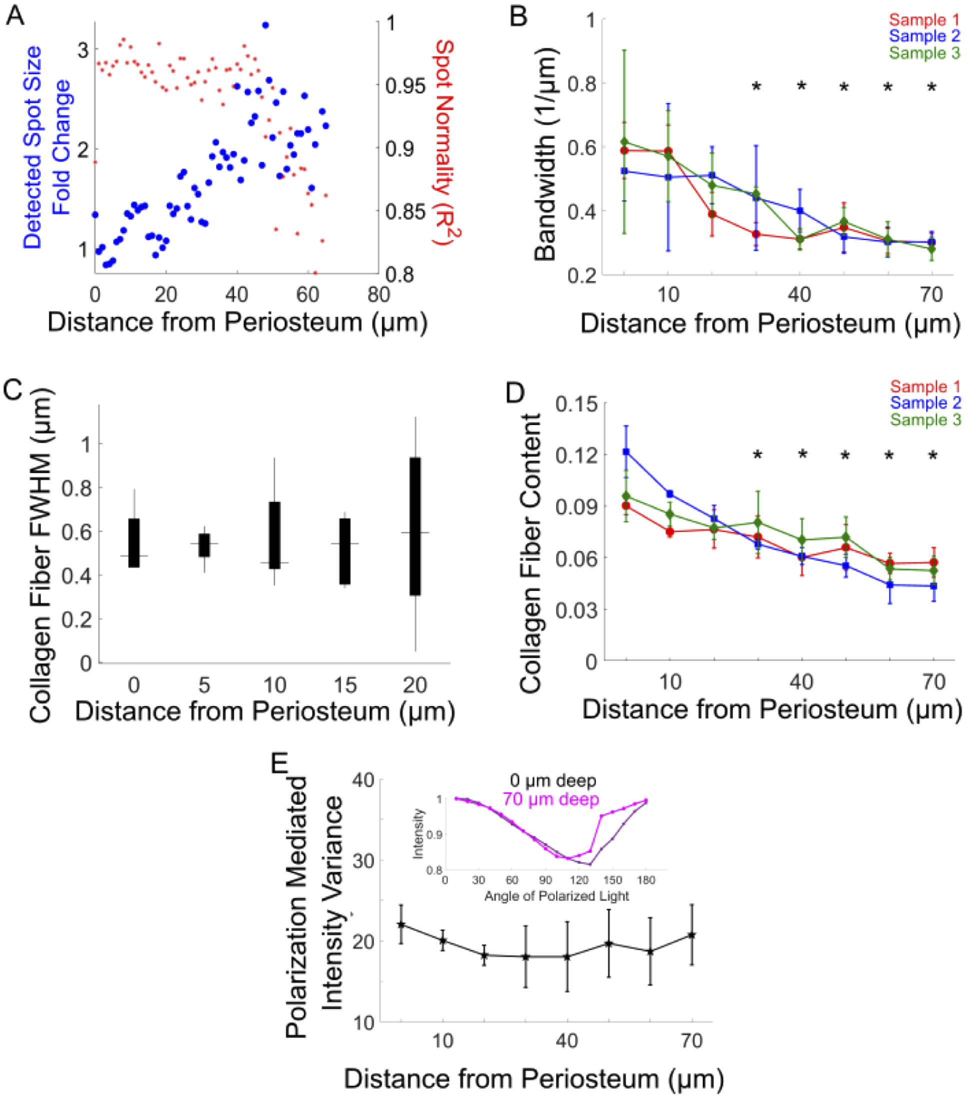

Fig. 3. Loss of resolution and maintenance of polarization through full thickness bone. (A) The detected spot size in bone gradually gets larger with depth while maintaining a Gaussian beam through the first mean-free-path of bone. (B) The bandwidth decreases with depth through 70 μm of adult bone. Significantly lower bandwidth than what is detected at 0 μm ($p < 0.05$) is denoted by (*). (C) The average collagen fiber width does not change over the first 20 μm of depth. (D) The amount of collagen fiber content that we are able to detect decreases with depth. Significantly less ($p < 0.05$) collagen fiber content than what is detected at 0 μm is denoted by (*). Each color represents a different calvarial bone sample with colors in (B) and (D) coordinating with each other. (E) The polarization contrast remains constant through 70 μm of adult bone. The standard deviation of all polarization stacks averaged 19.5% of the stack mean. Inset: Example normalized intensity values over angles of polarized light for images acquired at the surface (dark line) and 70 μm deep (light line).

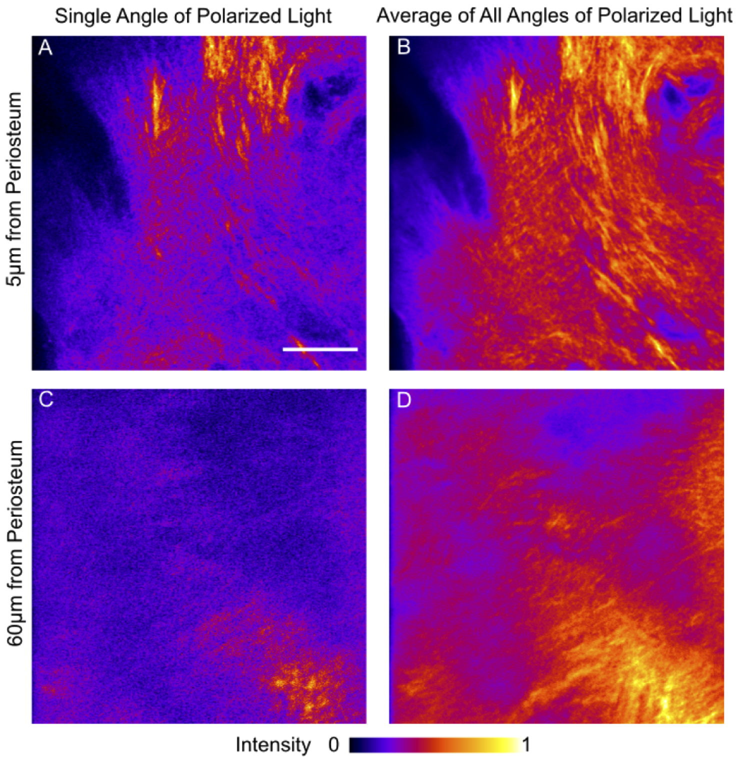

Fig. 4. Polarization is retained with depth while resolution diminishes. At 5 μm from the periosteum (A and B) in whole bone, more collagen fibers are visible than when bone is evaluated 60 μm from the periosteum (C and D). Polarized light selectively excites collagen fibers of a single orientation, here 30° to the vertical axis, regardless of depth in whole bone using SHG (A and C). When all angles of polarized light are used, collagen fibers of all orientations are more equally excited with SHG signal (B and D). Scale Bar: 20 μm.

could reduce the effective polarimetric contrast [13]. We therefore explored if the polarization contrast was retained in the apical 70 μm of the cranial bone by determining the polarization mediated intensity variance, which indicates the degree of intensity fluctuation created by modulating the polarization angle of excitation light. We found the average polarization mediated intensity variance across all depths was 19.5 ± 1.46% and there was no significant difference among any depths (Fig. 3(E)). By plotting an individual polarization response at 2 depths, we found that this similarity in the variance of polarimetric fluctuations was also associated with a similar shape profile of fluctuations (Fig. 3(E) inset).

To further probe the potential of SHG polarimetry to visualize regions of aligned collagen content, we normalized the intensities of a polarized SHG image. First we looked at an image from a single orientation of light, 30°, (Figs. 4(A) and 4(C)) and then we examined images that were the average intensity of all angles of polarized light (Figs. 4(B) and 4(D)). Collagen fibers are visible at 5 μm from the surface and collagen fibers of a single orientation are preferentially highlighted when only one angle of polarized light is used (Figs. 4(A) and 4(B)). Despite the expected decrease in resolution of individual fibrous structures at 50 μm into the bone, a similar level of polarimetric response of collagen fibers to a single orientation of polarized light is retained (Figs. 4(C) and 4(D)).

In the cranial bone, collagen is organized into sheets known as lamellar sheets that are stacked in disparate directions to provide mechanical stability, so we next imaged lamellar sheet orientation and stacking through depth. To provide a ground truth, we visualized lamella sheets in a freeze fractured skull using SEM (Fig. 5(A)). We visualized a single angle of excitation light in a normalized intensity x,z cross section and could observe variations in intensity suggesting layers of collagen fibers assembled into lamellar sheets with different orientations (Fig. 5(B)). Quantification of the intensity profile demonstrates the presence of these suspected lamellar sheets throughout the depth of the intact bone (Fig. 5(C)). However, the SHG intensity fluctuations visualized using one orientation of light could also be due to varying density of collagen fibers in the bone.

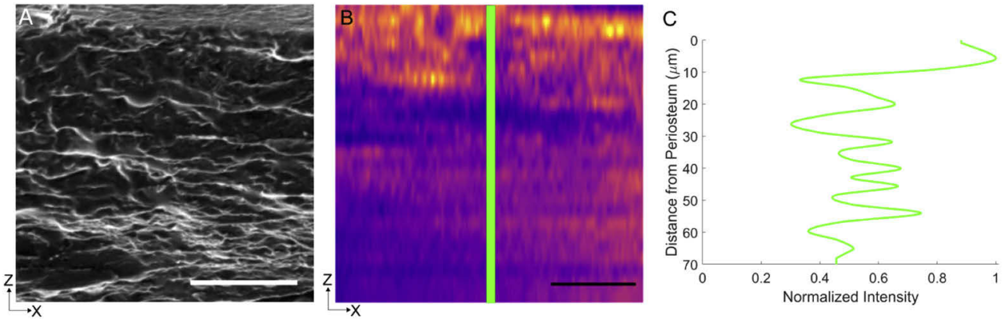

Fig. 5. Lamella sheet formation is observed through depth. (A) Freeze fractured cross sections of bone were analyzed with SEM to directly visualize lamella sheets. (B) An x,z profile of a single polarization of excitation light allows for visualization of lamella sheets in intact bone. Scale Bars: 20 μm. (C) Intensity profile of green line in (B) shows oscillatory patterns demonstrating alternating angles of lamella sheets.

4.1.2. Characterization of cranial bone anisotropy, polarization cross-talk, birefringence and diattentuation

Certain arrangements of ordered collagen fibers can cause distortions in the SHG polarimetric response, so we evaluated a group of potentially confounding factors for cranial bone imaging including anisotropy, polarization cross-talk, birefringence and diattenuation using the theoretical framework laid out in Section 2.2 and by Gusachenko et al. [32]. These experiments were conducted using the optical setup in Fig. 2(B).

We first sought to account for the difference in mean-free-paths between orthogonal orientations of light. We rotated polarized light over 180° every 10° every 5 μm of depth in full thickness bone from the surface to 70 μm and collected the x and y component of the epi-collected signal. To determine the diattenuation of SHG signal in intact bone, we found the mean-free-path at 0° and 90° from the x component to be 42.4 μm and 40.2 μm, respectively (Fig. 6(A)). These lengths are within roughly 5% of each other suggesting that diattenuation is not a strong contributor to the detected polarization state within the heterogeneous tissue of the bone.

The combined contributions of birefringence, $\Delta\varphi$, and polarization cross-talk, η, are intrinsically mixed and cannot be separated, so we determined their combined effect on the SHG signal as described by Gusachenko, et al. [32]. We first used Eq. (10) and demonstrated that ρ, the ratio of the two main tensorial components, remains relatively constant through the 70 μm of intact bone ($\rho = 0.47 \pm 0.16$; Fig. 6(B)) using three murine calvarial bones. Therefore, diattenuation contributes minimally to the epi-detected polarized light at all evaluated depths. Both $\Delta\varphi$ and η are defined by Δ; through the first 70 μm of intact bone, Δ equates to -0.079 ± 0.053 (Fig. 6(C)). Although small fluctuations in Δ are observed, these minimal contributions of birefringence are unlikely to significantly impact our estimation of collagen angular orientation. Defining these variables using our data (Fig. 6(D)) allowed us to describe the fit at each depth (Fig. 6(E)).

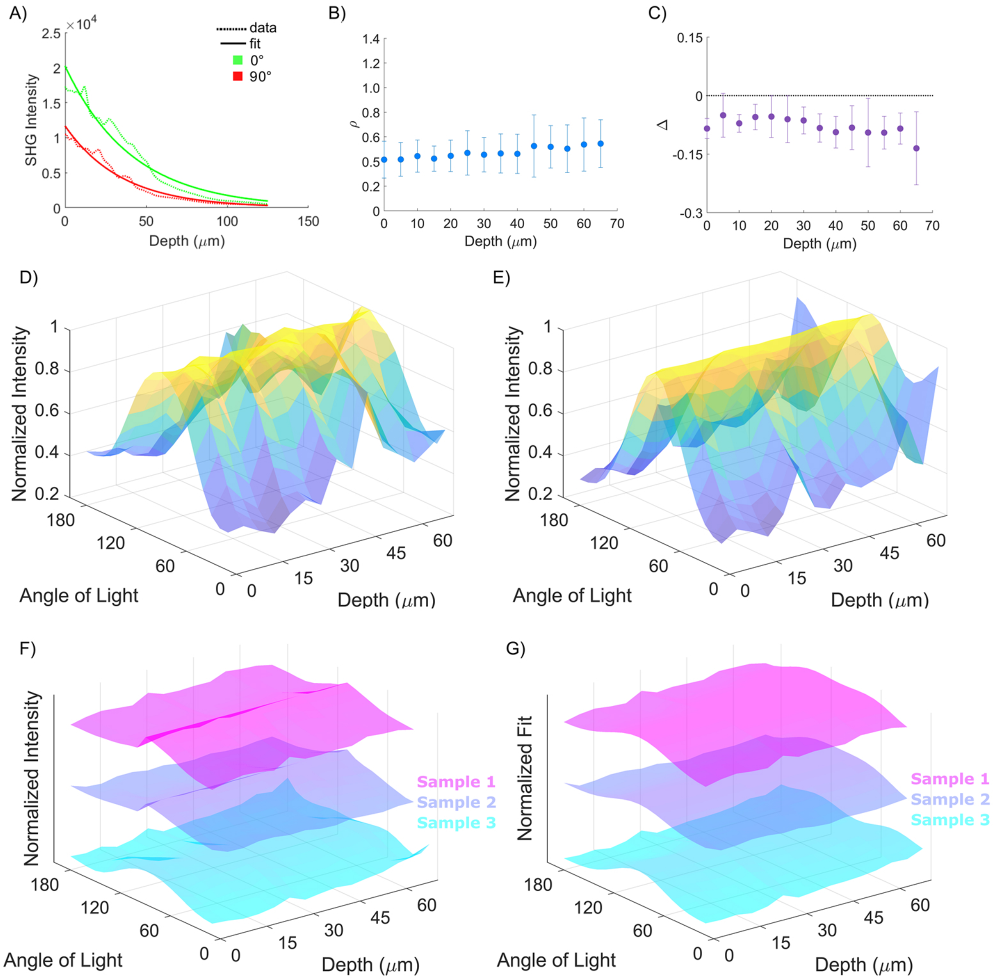

Fig. 6. Scattering properties of bone have little impact on polarization retention through the first mean-free-path. (A) The polarization angle of the excitation light is scattered similarly regardless of the angle of polarized light. (B) ρ, the ratio of the two main tensorial components, remains relatively constant through the depth of intact bone, though elevated by 70 μm of depth. (C) Δ is the combined effect of birefringence and polarization cross-talk; the combined effect exhibits small fluctuations through the depth of bone. (D) Linearly polarized light was rotated and the signal was collected through the depth of bone. (E) To examine the effects of birefringence and polarization cross-talk, our data was fitted using Eq. (13). (F) and (G) show similar trends in the normalized intensity and fit, respectively, across stacks acquired in 3 individual mice (each color represents one mouse). The data and fit are offset to allow for simultaneous viewing of the trends in each biological replicate.

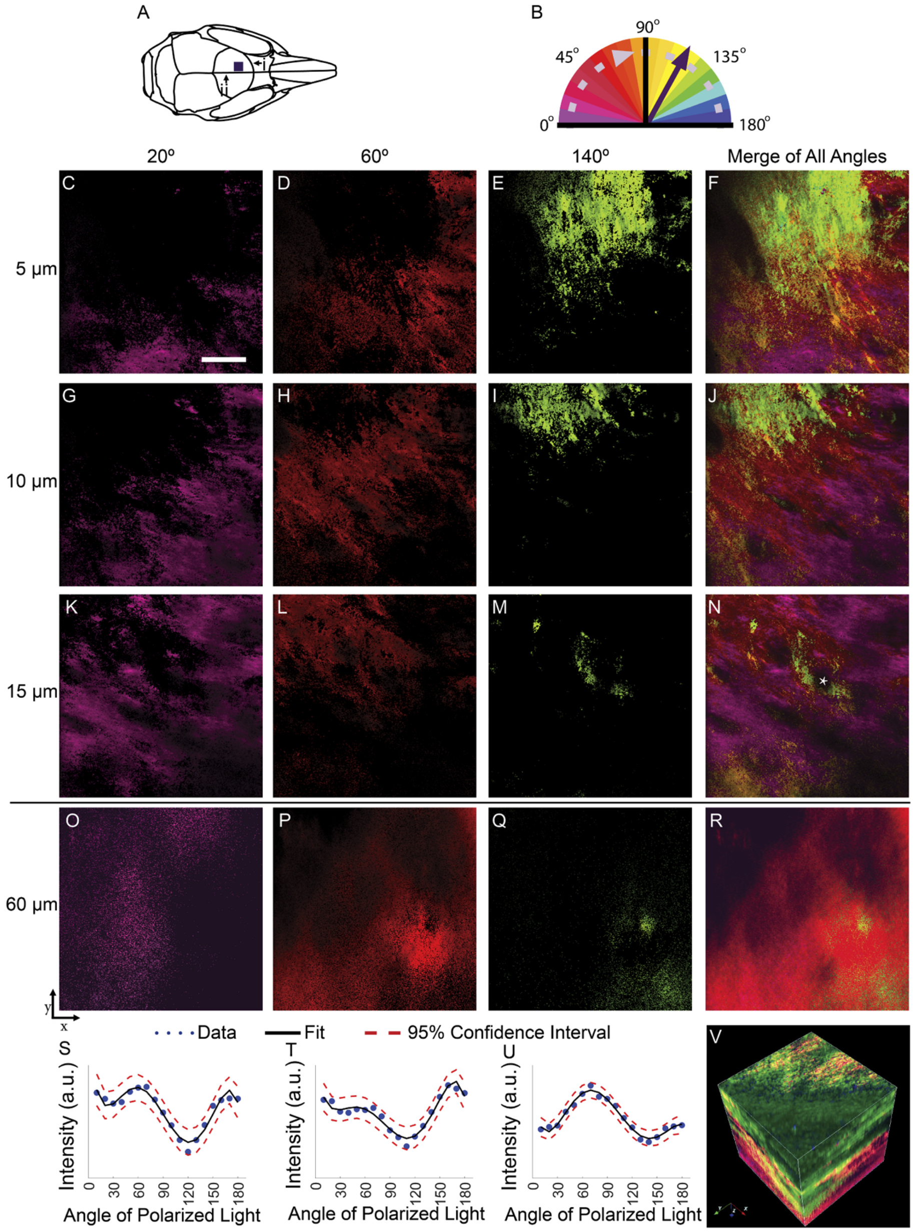

Fig. 7. SHG polarized imaging of collagen orientation in whole bone. (A) The frontal bones of wild type mice were imaged dorsal to the jugum limitans (i) and lateral to the sagittal suture (ii). (B) Polarized light was rotated using a motorized half-wave plate, images were collected every 10°, and pixels containing collagen fiber information were assigned colors based on orientation angle. Images were collected at 5 μm (C-F), 10 μm (G-J), 15 μm (K-N), and 60 μm (O-R) from the surface of the periosteum. The asterisk in N denotes an osteocyte lacunae. Scale Bar: 20 μm. (S-U) Average intensity profiles were plotted, fitted, and 95% confidence intervals were established to demonstrate the intensity signature of each orientation. (V) The same technique can be used to create a 3-D reconstruction of intact lamellar bone.

Additional biological replicates were analyzed and their normalized intensities were plotted with an offset to show multiple independent mouse experimental measures (Fig. 6(F)) and fitted values (Fig. 6(G)) showing an average Pearson's correlation coefficient between the experimental and modeling data of 0.88 ± 0.02.

4.2. *Angular distribution of collagen fibers in bone*

Since we found that the epi-detected SHG is minimally impacted by diattentuation, birefringence, and polarization cross-talk while imaging cranial bone collagen, we then evaluated the potential of SHG-polarimetric imaging to determine the dominant orientation of collagen fibers in the cranial bone tissue. For these experiments, the linear polarizer was removed from the detection arm and all orientations of SHG signal were collected in epi-detection.

We sacrificed two-week-old wild type mice and collected images of the whole cranial bone from regions lateral to the sagittal suture, anterior to the cranial suture, and posterior to the jugum limitans (Fig. 7(A)). The polarization angle of linearly polarized 775 nm femtosecond pulsed excitation light was rotated, and images were collected in the epi-orientation at every 10°, where 0° is defined as parallel with the sagittal suture. The orientation of collagen fibers was then determined on a pixel-by-pixel basis using Eq. (13). At 5-15 μm and 60 μm from the surface of the bone, every 10° was assigned a representative color to provide discrimination between collagen fibers of different orientations in the dense bone structure (Fig. 7(B)).

Spatially co-localized groups of fibers of similar orientation can be seen throughout the depth of the bone, as indicated by conserved patterns of color (Figs. 7(C)-7(R)). Sequential images acquired with 5 μm axial steps are delineated by orientation angles conserved over multiple imaging planes, such as the grouped yellow-green structures in Figs. 7(E) and 7(I), suggesting the fibers are organized into lamellar sheet structures. Likewise, Fig. 7(N) clearly shows an SHG-dim osteocyte lacunae (marked with asterisk) surrounded by collagen fibers organized into circular patterns. The intensity profiles of representative angle-specific pixels at each depth were plotted (Figs. 7(S)–7(U)), and at each angle of collagen orientation, there is a signature SHG intensity response to the polarimetric light.

This technique was used to acquire images of cranial bone at 1 μm axial intervals through the bone and reconstruct 3-D structures (Fig. 7(V)). As in the 2-D images, we visualized lamellar sheet organization in the apical 70 μm of the bone. Regions of similarly oriented collagen fibers, and thus comparable colors, were visualized with many fibers oriented parallel to the sagittal suture. This analysis highlights the 3-D nature of the organization of deposited collagen to visualize of the collagen lamellar sheet structures in healthy intramembranous bone.

5. Discussion

This work demonstrates the use of SHG polarimetric analysis to characterize the assembly of collagen fibers in the cranial bones in lamellar sheet structures. Our technique could enable the monitoring of bone quality during states of disease and regeneration. SHG polarimetric analysis has not been commonly used for intact whole bone, in part due to rapid loss of signal with depth and concerns about the impact of the heterogeneous bone tissue on polarimetric measures. Here, despite the significant reduction in focal spot quality, the polarization of the excitation light was not as strongly impacted throughout the first 70 μm of the bone as the resolution, suggesting that polarimetric SHG imaging could be potentially useful for evaluating collagen production and organization in mouse cranial bone.

To evaluate collagen content and structure, typically a tissue biopsy undergoes thin sectioning, histological staining (e.g. von Kossa), and analysis by highly trained pathologists [20,36]. This approach limits sampling to a small 2-D area and is not easily quantifiable [20]. SEM is an alternative strategy with adequate resolution and contrast to identify individual collagen bundles as well as their assembled lamellar sheets, but is significantly time- and labor-intensive and is not conducive to volumetric or quantitative analysis [14]. Our work therefore builds on existing approaches to create a non-invasive 3-D technique to describe bone collagen organization.

We investigated the potential distortions of SHG signal that often arise from secondary organization of collagen fibers in tissues such as tendons [28] using polarization-resolved-detection analysis of the SHG signal to more closely investigate potential confounding factors for our polarimetric imaging. In the mouse cranial bone we do not find evidence of substantial alteration of the polarimetric response by diattenuation [37], birefringence [38], and polarization cross-talk [32]. While the highly scattering properties of bone create an exponential decay in the intensity of back-detected signal, the attenuation lengths of parallel and perpendicular excitation light are similar, which yields a ratio of the two main tensorial components, ρ, that remains relatively constant through the first 60-70 μm of intact bone, with a value near 0.47. This value varied somewhat from animal to animal with average values ranging from 0.4-0.7, but remained fairly constant within an animal ± 0.1 across different optical sections and imaging locations. Animal to animal variability could potentially have been related to slight differences in animal age or sample preparation that might impact the collagen fiber extension. In the bone, the crosslinking of the collagen could explain the slightly lower ρ average values we found than what has been reported in the ovary [37], c. elegans and muscle [10], and 0.71 in tendon [32]. In addition, the Δ parameter exhibits low amounts of oscillation over depth, suggesting that there is little impact of birefringence in our sample. Thus we can conclude that the polarimetric back-detected signal is not excessively distorted and retains much of the expected polarization information. Unlike aligned collagen fibers in tendons, which have been a primary tissue of study for thick tissue SHG [32], the highly heterogeneous bone tissue has numerous orientations of fibers organized into lamella sheets thus explaining the lower ρ. In tissues such as the tendon these confounding factors strongly impact the detected polarimetric signal and require correction to extract collagen features [32]. Our current analysis is limited to cranial bones, and future work that aims to transition these findings into long bones may have to account for the aligned secondary structures like Haversian canals that likely will impact polarimetric readouts.

It is of practical concern to understand the maximum imaging depth that retains polarization information and bone quality features. We found a substantial reduction in the power spectral density and frequency content by 30 μm of depth in the bone, but enough of the polarization information was retained to provide polarimetric contrast between differently oriented portions of the images as deep as 70 μm. Although most human bones are much thicker than 70 μm, the insufficiency fractures that characterize fragile bones have been associated with crack propagation from the bone surface. Such fractures are normally arrested close to the bone surface by the collagen mesh before they propagate deeper into the bone structure. Therefore, imaging collagen mesh structure near the bone surface could provide meaningful insight into crack arrest and propagation risk [39]. This fibrous collagen structure provides critical toughness to the bone that helps to prevent crack propagation and has key functional properties near the bone surface. However, deeper imaging could provide more structural information about underlying bone layers. As our previous work has examined, low order aberrations and high order tissue scattering strongly impact the quality of the excitation beam focal spot deep in the bone [30]. In order to increase the imaging penetration for deeper polarimetric analysis of collagen in highly scattering bone tissue, aberration and scattering correction strategies must be implemented using adaptive optical elements [30,40–43]. Still, the fundamental limitations of optical scattering are likely to confine SHG analysis to features near the surface of the bone.

While disorganized regions still exist in the young adult bones used throughout much of this work, the presence of well-organized lamella sheets suggest that the bone is nearing completion of remodeling from a woven to a lamellar state. In healthy bone, collagen molecules are excreted from osteoblasts and self-assemble into parallel fibrils with gaps between the ends of the molecules that are filled with hydroxyapatite [8]. Therefore, the study of collagen, including its lateral spatial orientation, could provide insight into the bone mineralization process. SHG-evaluated collagen properties may be associated with bone mechanical properties, especially toughness and crack defect stabilizing capabilities [44]. Furthermore, in previous studies that aim to examine collagen fiber secondary organization in bone, the tissue has been decalcified or cleared, embedded, and sectioned into pieces several microns thick [45–47]. Sectioning strategies are time consuming and decrease the available spatial information about the tissue, which our polarimetric SHG approach is able to retain. Therefore, our approach could potentially provide insight in non-damaging and label-free imaging that could be performed in living patients to assist with traditional bone quality metrics like bone mineral density that fail to predict fracture risk in age-related and bone-fragility diseases due to the mechanical contributions of the collagen fiber mesh [39,48,49].

Changes in bone collagen composition have been suggested to be a risk factor for osteoporotic fractures [50–52] and alterations in collagen cross-links have been seen in osteoporotic cortical [53] and trabecular bone [50]. Postmenopausal women have thinner cortices and higher porosity of the cortical bone in their femurs [54]. Non-enzymatic cross-linking of collagen is prominent in diseased and aged bone and negatively impacts collagen's ability to dissipate energy, thus increasing fracture risk [55]. Thus, the results of this technique indicate that it could potentially be relevant for whole osteoporotic bone and could aid in the diagnosis and assessment of treatment in diseased bone.

6. Conclusion

Our results presented in this work indicate the potential of SHG imaging to understand and quantify collagen fiber organization into lamellar sheet structures in intact whole bone tissue. We evaluated the impact of diattenuation, birefringence, and polarization cross-talk on the back-detected polarized SHG signal and demonstrated that the influence of these parameters is negligible within the first mean-free-path of bone and minimal in the second mean-free-path. We have identified the dominant orientation angles of collagen fibers in the cranial bone using polarimetric nonlinear excitation. In healthy cranial bone, fiber angles tend to group into regions within an axial plane and throughout neighboring axial planes. By identifying these features in 3-D, we are able to clearly denote regions of collagen alignment where modeling and remodeling of collagen and mineral produces structures resembling lamellar sheets in healthy wild type mice [8]. This method can be expanded to studying other whole tissues and can be employed with traditional bone mineral density evaluation to assess bone health. Our work demonstrates the ability to detect the angle of collagen orientation more comprehensively in full thickness bone with polarized SHG signal beyond the first mean-free-path.

Funding

National Science Foundation (1706916); National Institutes of Health (R21 Trailblazer #1R21EB027802-01); Regenerative Engineering and Medicine Georgia Partners in Medicine; Soft Bones (Maher Family Research Grant).

Disclosures

The authors declare no conflicts of interest.

References

1. S. R. Stock, "The mineral–collagen interface in bone," Calcif. Tissue Int. **97**(3), 262–280 (2015).
2. R. Christensen, *Mechanics of Composite Materials* (Krieger, 1991).
3. M. Saito and K. Marumo, "Collagen cross-links as a determinant of bone quality: a possible explanation for bone fragility in aging, osteoporosis, and diabetes mellitus," Osteoporosis Int. **21**(2), 195–214 (2010).
4. M. Saito, Y. Kida, S. Kato, and K. Marumo, "Diabetes, collagen, and bone quality," Curr. Osteoporos Rep. **12**(2), 181–188 (2014).

5. A. Forlino and J. C. Marini, "Osteogenesis imperfecta," Lancet **387**(10028), 1657–1671 (2016).
6. G. Cox, E. Kable, A. Jones, I. Fraser, F. Manconi, and M. D. Gorrell, "3-dimensional imaging of collagen using second harmonic generation," J. Struct. Biol. **141**(1), 53–62 (2003).
7. X. Chen, O. Nadiarynkh, S. Plotnikov, and P. J. Campagnola, "Second harmonic generation microscopy for quantitative analysis of collagen fibrillar structure," Nat. Protoc. **7**(4), 654–669 (2012).
8. J. Y. Rho, L. Kuhn-Spearing, and P. Zioupos, "Mechanical properties and the hierarchical structure of bone," Med. Eng. Phys. **20**(2), 92–102 (1998).
9. Z. Zhou, D. Qian, and M. Minary-Jolandan, "Molecular mechanism of polarization and piezoelectric effect in super-twisted collagen," ACS Biomater. Sci. Eng. **2**(6), 929–936 (2016).
10. P. J. Campagnola and L. M. Loew, "Second-harmonic imaging microscopy for visualizing biomolecular arrays in cells, tissues and organisms," Nat. Biotechnol. **21**(11), 1356–1360 (2003).
11. B. Alberts, A. Johnson, J. Lewis, M. Raff, K. Roberts, and P. Walter, *Molecular Biology of the Cell* (Garland Science, 2002).
12. I. Jager and P. Fratzl, "Mineralized collagen fibrils: a mechanical model with a staggered arrangement of mineral particles," Biophys. J. **79**(4), 1737–1746 (2000).
13. M. A. Houle, C. A. Couture, S. Bancelin, J. Van der Kolk, E. Auger, C. Brown, K. Popov, L. Ramunno, and F. Legare, "Analysis of forward and backward second harmonic generation images to probe the nanoscale structure of collagen within bone and cartilage," J. Biophotonics **8**(11-12), 993–1001 (2015).
14. R. Ambekar, M. Chittenden, I. Jasiuk, and K. C. Toussaint Jr., "Quantitative second-harmonic generation microscopy for imaging porcine cortical bone: comparison to sem and its potential to investigate age-related changes," Bone **50**(3), 643–650 (2012).
15. R. Genthial, E. Beaurepaire, M.-C. Schanne-Klein, F. Peyrin, D. Farlay, C. Olivier, Y. Bala, G. Boivin, J.-C. Vial, D. Débarre, and A. Gourrier, "Label-free imaging of bone multiscale porosity and interfaces using third-harmonic generation microscopy," Sci. Rep. **7**(1), 3419 (2017).
16. T. Tang, V. Ebacher, P. Cripton, P. Guy, H. McKay, and R. Wang, "Shear deformation and fracture of human cortical bone," Bone **71**, 25–35 (2015).
17. T. Yasui, Y. Tohno, and T. Araki, "Determination of collagen fiber orientation in human tissue by use of polarization measurement of molecular second-harmonic-generation light," Appl. Opt. **43**(14), 2861–2867 (2004).
18. W. Lee, H. Rahman, M. E. Kersh, and K. C. Toussaint Jr., "Application of quantitative second-harmonic generation microscopy to posterior cruciate ligament for crimp analysis studies," J. Biomed. Opt. **22**(4), 046009 (2017).
19. P. J. Campagnola, A. C. Millard, M. Terasaki, P. E. Hoppe, C. J. Malone, and W. A. Mohler, "Three-dimensional high-resolution second-harmonic generation imaging of endogenous structural proteins in biological tissues," Biophys. J. **82**(1), 493–508 (2002).
20. P. Campagnola, "Second harmonic generation imaging microscopy: Applications to diseases diagnostics," Anal. Chem. **83**(9), 3224–3231 (2011).
21. E. Ralston, B. Swaim, M. Czapiga, W. L. Hwu, Y. H. Chien, M. G. Pittis, B. Bembi, O. Schwartz, P. Plotz, and N. Raben, "Detection and imaging of non-contractile inclusions and sarcomeric anomalies in skeletal muscle by second harmonic generation combined with two-photon excited fluorescence," J. Struct. Biol. **162**(3), 500–508 (2008).
22. D. T. Fung, J. B. Sereysky, J. Basta-Pljakic, D. M. Laudier, R. Huq, K. J. Jepsen, M. B. Schaffler, and E. L. Flatow, "Second harmonic generation imaging and fourier transform spectral analysis reveal damage in fatigue-loaded tendons," Ann. Biomed. Eng. **38**(5), 1741–1751 (2010).
23. O. Nadiarnykh, S. Plotnikov, W. A. Mohler, I. Kalajzic, D. Redford-Badwal, and P. J. Campagnola, "Second harmonic generation imaging microscopy studies of osteogenesis imperfecta," J. Biomed. Opt. **12**(5), 051805 (2007).
24. K. Tilbury, C.-H. Lien, S.-J. Chen, and P. J. Campagnola, "Differentiation of col i and col iii isoforms in stromal models of ovarian cancer by analysis of second harmonic generation polarization and emission directionality," Biophys. J. **106**(2), 354–365 (2014).
25. R. Lacomb, O. Nadiarnykh, and P. J. Campagnola, "Quantitative second harmonic generation imaging of the diseased state osteogenesis imperfecta: experiment and simulation," Biophys. J. **94**(11), 4504–4514 (2008).
26. J. C. Mansfield, V. Mandalia, A. Toms, C. P. Winlove, and S. Brasselet, "Collagen reorganization in cartilage under strain probed by polarization sensitive second harmonic generation microscopy," J. R. Soc., Interface **16**(150), 20180611 (2019).
27. F. Aptel, N. Olivier, A. Deniset-Besseau, J.-M. Legeais, K. Plamann, M.-C. Schanne-Klein, and E. Beaurepaire, "Multimodal nonlinear imaging of the human cornea," Invest. Ophthalmol. Visual Sci. **51**(5), 2459–2465 (2010).
28. Y. Goulam Houssen, I. Gusachenko, M. C. Schanne-Klein, and J. M. Allain, "Monitoring micrometer-scale collagen organization in rat-tail tendon upon mechanical strain using second harmonic microscopy," J. Biomech. **44**(11), 2047–2052 (2011).
29. R. Turcotte, J. M. Mattson, J. W. Wu, Y. Zhang, and C. P. Lin, "Molecular order of arterial collagen using circular polarization second-harmonic generation imaging," Biophys. J. **110**(3), 530–533 (2016).
30. K. F. Tehrani, P. Kner, and L. J. Mortensen, "Characterization of wavefront errors in mouse cranial bone using second-harmonic generation," J. Biomed. Opt. **22**(3), 036012 (2017).
31. C. Teulon, I. Gusachenko, G. Latour, and M.-C. Schanne-Klein, "Theoretical, numerical and experimental study of geometrical parameters that affect anisotropy measurements in polarization-resolved SHG microscopy," Opt. Express **23**(7), 9313–9328 (2015).

32. I. Gusachenko, G. Latour, and M. C. Schanne-Klein, “Polarization-resolved second harmonic microscopy in anisotropic thick tissues,” Opt. Express **18**(18), 19339–19352 (2010).
33. C.-H. Lien, K. Tilbury, S.-J. Chen, and P. J. Campagnola, “Precise, motion-free polarization control in second harmonic generation microscopy using a liquid crystal modulator in the infinity space,” Biomed. Opt. Express **4**(10), 1991–2002 (2013).
34. K. F. Tehrani, J. Xu, Y. Zhang, P. Shen, and P. Kner, “Adaptive optics stochastic optical reconstruction microscopy (ao-storm) using a genetic algorithm,” Opt. Express **23**(10), 13677–13692 (2015).
35. S. Weiner, W. Traub, and H. D. Wagner, “Lamellar bone: structure-function relations,” J. Struct. Biol. **126**(3), 241–255 (1999).
36. C. P. Adler, *Bone Diseases: Macroscopic, Histological, and Radiological Diagnosis of Structural Changes in the Skeleton* (Springer Science and Business Media, 2013).
37. P. Stoller, K. M. Reiser, P. M. Celliers, and A. M. Rubenchik, “Polarization-modulated second harmonic generation in collagen,” Biophys. J. **82**(6), 3330–3342 (2002).
38. D. Ait-Belkacem, A. Gasecka, F. Munhoz, S. Brustlein, and S. Brasselet, “Influence of birefringence on polarization resolved nonlinear microscopy and collagen SHG structural imaging,” Opt. Express **18**(14), 14859–14870 (2010).
39. C. Acevedo, V. A. Stadelmann, D. P. Pioletti, T. Alliston, and R. O. Ritchie, “Fatigue as the missing link between bone fragility and fracture,” Nat. Biomed. Eng. **2**(2), 62–71 (2018).
40. J. H. Park, W. Sun, and M. Cui, “High-resolution in vivo imaging of mouse brain through the intact skull,” Proc. Natl. Acad. Sci. U. S. A. **112**(30), 9236–9241 (2015).
41. D. B. Conkey, A. M. Caravaca-Aguirre, and R. Piestun, “High-speed scattering medium characterization with application to focusing light through turbid media,” Opt. Express **20**(2), 1733–1740 (2012).
42. Q. Feng, B. Zhang, Z. Liu, C. Lin, and Y. Ding, “Research on intelligent algorithms for amplitude optimization of wavefront shaping,” Appl. Opt. **56**(12), 3240–3244 (2017).
43. J. Tang, R. N. Germain, and M. Cui, “Superpenetration optical microscopy by iterative multiphoton adaptive compensation technique,” Proc. Natl. Acad. Sci. U. S. A. **109**(22), 8434–8439 (2012).
44. P. Garnero, “The role of collagen organization on the properties of bone,” Calcif. Tissue Int. **97**(3), 229–240 (2015).
45. J. Caetano-Lopes, A. M. Nery, H. Canhão, J. Duarte, R. Cascão, A. Rodrigues, I. P. Perpétuo, S. Abdulghani, P. M. Amaral, S. Sakaguchi, Y. T. Konttinen, L. Graça, M. F. Vaz, and J. E. Fonseca, “Chronic arthritis leads to disturbances in the bone collagen network,” Arthritis Res. Ther. **12**(1), R9 (2010).
46. R. C. Paietta, E. L. Burger, and V. L. Ferguson, “Mineralization and collagen orientation throughout aging at the vertebral endplate in the human lumbar spine,” J. Struct. Biol. **184**(2), 310–320 (2013).
47. S. Ranjit, A. Dvornikov, M. Stakic, S.-H. Hong, M. Levi, R. M. Evans, and E. Gratton, “Imaging fibrosis and separating collagens using second harmonic generation and phasor approach to fluorescence lifetime imaging,” Sci. Rep. **5**(1), 13378 (2015).
48. S. L. Hui, C. W. Slemenda, and C. C. Johnston Jr, “Age and bone mass as predictors of fracture in a prospective study,” J. Clin. Invest. **81**(6), 1804–1809 (1988).
49. S. C. Schuit, M. van der Klift, A. E. Weel, C. E. de Laet, H. Burger, E. Seeman, A. Hofman, A. G. Uitterlinden, J. P. van Leeuwen, and H. A. Pols, “Fracture incidence and association with bone mineral density in elderly men and women: the rotterdam study,” Bone **34**(1), 195–202 (2004).
50. E. P. Paschalis, E. Shane, G. Lyritis, G. Skarantavos, R. Mendelsohn, and A. L. Boskey, “Bone fragility and collagen cross-links,” J. Bone Miner. Res. **19**(12), 2000–2004 (2004).
51. D. J. Prockop and K. I. Kivirikko, “Collagens: molecular biology, diseases, and potentials for therapy,” Annu. Rev. Biochem. **64**(1), 403–434 (1995).
52. A. J. Bailey, S. F. Wotton, T. J. Sims, and P. W. Thompson, “Biochemical changes in the collagen of human osteoporotic bone matrix,” Connect. Tissue Res. **29**(2), 119–132 (1993).
53. E. F. Holland, J. W. Studd, J. P. Mansell, A. T. Leather, and A. J. Bailey, “Changes in collagen composition and cross-links in bone and skin of osteoporotic postmenopausal women treated with percutaneous estradiol implants,” Obstet Gynecol. **83**, 180–183 (1994).
54. R. Shigdel, M. Osima, L. A. Ahmed, R. M. Joakimsen, E. F. Eriksen, R. Zebaze, and A. Bjornerem, “Bone turnover markers are associated with higher cortical porosity, thinner cortices, and larger size of the proximal femur and non-vertebral fractures,” Bone **81**, 1–6 (2015).
55. A. A. Poundarik, P. C. Wu, Z. Evis, G. E. Sroga, A. Ural, M. Rubin, and D. Vashishth, “A direct role of collagen glycation in bone fracture,” J. Mech. Behav. Biomed. Mater. **52**, 120–130 (2015).